7-2-2020

Improving Thermal Conduction Across Cathode/Electrolyte Interfaces in Solid-State Lithium-Ion Batteries by Hierarchical Hydrogen-Bond Network

Jinlong He
Utah State University

Lin Zhang
University of Pittsburgh

Ling Liu
Temple University

Recommended Citation

He, J., Zhang, L., Liu, L. 2020. Improving thermal conduction across cathode/electrolyte interfaces in solid-state lithium-ion batteries by hierarchical hydrogen-bond network. Materials & Design. Vol. 194. 1-10. https://doi.org/10.1016/j.matdes.2020.108927

Materials and Design 194 (2020) 108927

Contents lists available at ScienceDirect

Materials and Design

journal homepage: www.elsevier.com/locate/matdes

Improving thermal conduction across cathode/electrolyte interfaces in solid-state lithium-ion batteries by hierarchical hydrogen-bond network

Jinlong He [a,b], Lin Zhang [c], Ling Liu [a,*]

[a] Department of Mechanical Engineering, Temple University, Philadelphia, PA 19122, United States
[b] Department of Mechanical and Aerospace Engineering, Utah State University, Logan, UT 84322, United States
[c] Department of Mechanical Engineering and Materials Science, University of Pittsburgh, Pittsburgh, PA 15261, United States

HIGHLIGHTS

- Electrode/electrolyte interfaces are decorated with self-assembled monolayers for drastically improved thermal transport
- Self-assembled monolayers uniquely feature hierarchical hydrogen-bond networks that introduce new thermal transport pathways
- Interfacial thermal conduction is drastically enhanced by approximately 211.69% according to molecular dynamics simulations
- Results may guide interface engineering to significantly improve thermal management and safety of batteries

GRAPHICAL ABSTRACT

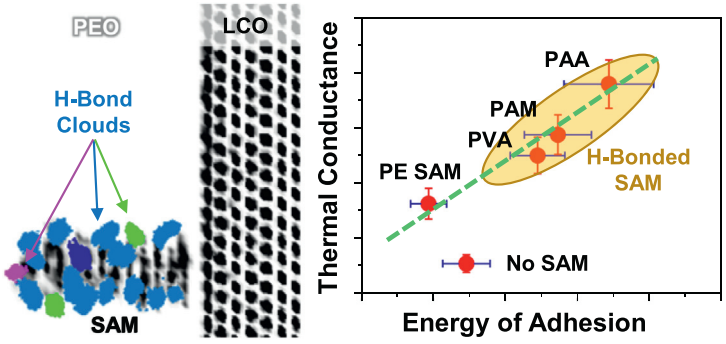

ARTICLE INFO

Article history:
Received 5 March 2020
Received in revised form 24 June 2020
Accepted 25 June 2020
Available online 02 July 2020

Keywords:
Solid-state lithium-ion batteries
Self-assembled monolayers
Interfacial thermal conductance
Hydrogen bonding
Molecular dynamics

ABSTRACT

Effective thermal management is an important issue to ensure safety and performance of lithium-ion batteries. Fast heat removal is highly desired but has been obstructed by the high thermal resistance across cathode/electrolyte interface. In this study, self-assembled monolayers (SAMs) are used as the vibrational mediator to tune interfacial thermal conductance between an electrode, lithium cobalt oxide (LCO), and a solid state electrolyte, polyethylene oxide (PEO). Embedded at the LCO/PEO interface, SAMs are specially designed to form hierarchical hydrogen-bond (H-bond) network with PEO. Molecular dynamics simulations demonstrate that all SAM-decorated interfaces show enhanced thermal conductance and dominated by H-bonds types. The incorporation of poly(acrylic acid) (PAA) SAM drastically enhances interfacial thermal conductance by approximately 211.69%, largely due to the formation of a strong H-bond, -COOH···:O, between PAA and PEO. Even with weaker H-bonds such as -OH···:O, it still outperforms the pristine interface as well as interfaces decorated with non-H-bonded SAMs, e.g. PE. Such improvement is attributed to the unique hierarchical H-bond network at the interface, which removes discontinuities in temperature field, straighten SAM chains, make materials strongly adhere, and couple the vibrational modes of materials. The study is expected to guide surface engineering for more effective thermal management in lithium-ion batteries.

Abbreviations: MD, molecular dynamics; NEMD, non-equilibrium molecular dynamics; RNEMD, reverse non-equilibrium molecular dynamics; SAM, self-assembled monolayer; LCO, lithium cobalt oxide ($LiCoO_2$); PEO, poly(ethylene oxide); PE, polyethylene; PVA, poly(vinyl alcohol); PAM, polyacrylamide; PAA, poly(acrylic acid); VDOS, the vibrational density of states..

* Corresponding author.
E-mail address: ling.liu@temple.edu (L. Liu).

https://doi.org/10.1016/j.matdes.2020.108927

1. Introduction

Solid-state lithium-ion batteries have been widely employed for applications including consumer electronics and electric vehicles for their high energy density, specific capacity and credible life [1,2]. Many novel materials have been developed in recent years for the cathode, anode and electrolyte of solid-state lithium-ion batteries to achieve high electrochemical performance. Despite the progress, applications and deployment of solid-state lithium-ion batteries are also influenced by other issues such as the thermal management [3]. As batteries are in operation, heat builds up and if not dissipated efficiently, it may cause overheating leading to lower electrochemical performance and even thermal runway [4–8]. To address this issue, several methods have been proposed including overdesigning, less operation and reducing interfacial impedance by thermal treatment to keep the battery temperature below the design limit. While being effective, these approaches inevitably reduce the efficiency or increase the cost of batteries.

An alternative and arguably more fundamental approach is to enhance the intrinsic thermal conductivity of lithium-ion batteries, making heat removal more efficient [9]. Previous studies in lithium-ion batteries have discovered that the actual bottleneck obstructing heat transfer in lithium-ion batteries is the interfaces between the material components [10–12]. Indeed, a recent experiment [13] in lithium-ion batteries has shown that, with thermal resistance of about 840 μK m^2 W^{-1}, interface contributes over 88% to the overall thermal resistance of lithium-ion batteries. Hence, it becomes imperative to enhance thermal conduce across materials interfaces to make heat transfer in solid-state lithium-ion batteries more efficient.

Material interfaces are thermally resistant because significant scattering takes place while phonons transport from one material into another. The interfacial phonon scattering has been shown to strongly correlate with the mismatch between the phonon states of two materials as well as the interfacial strength. As such, many approaches have been developed to reduce phonon scattering and improve interfacial heat transfer, including enhancing the interfacial adhesion [14–16], increasing stiffness [17,18], strengthening interfacial interactions [10,19], matching phonon modes [20–22] and functionalizing surfaces [23,24].

This study aims to reduce thermal resistance across the cathode/electrolyte interface by incorporating a hierarchical network of H-bonds enabled by polymeric self-assembled monolayers (SAMs). Organizing molecular assemblies into large ordered domains on surfaces, SAMs have attracted extensive attention due to its wide applications in many fields such as wetting and adhesion [25–27], nanofabrication [28], biocompatibility and molecular recognition [29], nanostructure deposition [30], and interface engineering [31–33]. The interfacial modification represents a unique combination of two novel concepts that have been previously shown to enhance interfacial thermal transport across various materials interfaces: (1) adding a polymeric monolayer between the two materials forming an interface and (2) designing interfaces to carry H-bonds. On one hand, self-assembled monolayer (SAM) has been widely investigated to improve interfacial thermal conduction between metals [20,21] and across graphene/polymer interfaces [34]. In particular, the interfacial thermal conductance has been shown to largely depend on the strength of the chemical bonds associated with the SAM [20,35]. For instance, at the interface between quartz and gold, the SAM with SH-C_{11}-Si ≡ increases thermal conductance by 80%, much more than other SAMs with weaker bonds at the interface. On the other hand, incorporating H-bonds has drastically enhanced thermal conduction in several materials systems including crystalline polymer nanofibers [36], protein β-sheets [37,38], polymer blends [39], graphene/polymer interface [34] and solid/liquid interfaces [35,40]. The H-bond is a strong secondary chemical bond formed between a hydrogen atom bound to a more electronegative atom or group (H-bond donor) and a nearby atom that serves as the H-bond acceptor. One of its unique advantages is that it has higher strength than the van der Waals interaction [41]. By functionalizing graphene with hydroxyl groups at the graphene/PMMA interface, H-bonds form and enable new thermal transport pathways, leading to a significant increase of 273% for the interfacial thermal conductance.

By combining the unique features of both SAMs and the H-bonding, this work probes the use of H-bonded SAMs for improved interfacial thermal transport across cathode/electrolyte interfaces. The cathode material under investigation is lithium cobalt oxide ($LiCoO_2$ or LCO) [42] and the solid electrolyte material is poly(ethylene oxide) (PEO). Both are widely used in commercial solid-state lithium-ion batteries for portable devices. Molecular dynamics simulation shows that specially designed H-bonded SAMs can enhance the interfacial thermal conductance by over 200%. The level of enhancement depends strongly on the type and density of H-bonds carried by different SAMs. For example, the LCO-PAA/PEO interface which features the primary H-bond of -COOH···:O drastically enhances the interfacial thermal conductance by 211.69%, while the LCO-PVA/PEO interface which has a different type of primary H-bond, -OH···:O, shows a relatively lower enhancement of 127.36%. Both are higher than the enhancement of 70.57% given by the PE SAM which carries no H-bonding.

2. Models and methods

2.1. Cathode/electrolyte interface models

Fig. 1a shows an atomistic model with four symmetric cathode/electrolyte (LCO/PEO) interfaces. The computational system has a size of 42.161 Å × 34.136 Å × 258.512 Å. Four kinds of polymeric SAMs were used to functionalize the LCO surface including polyethylene (PE, $[C_2H_4]_n$), polyvinyl alcohol (PVA, $[C_2H_4O]_n$), polyacrylamide (PAM, $[C_3H_5NO]_n$) and polyacrylic acid (PAA, $[C_3H_4O_2]_n$), as illustrated in Fig. 1b. The four SAMs have almost the same length for backbone consisting six repeat units, and they have distinct side chains. The PE has $–CH_3$ side chains which do not form H-bonds with PEO. The other three all form H-bonds with PEO, but the formed H-bonds have different numbers and strengths. The primary H-bonds formed at these interfaces are illustrated in the inset images of Fig. 1c. For the LCO-PVA/PEO interface, the primary H-bond forms between the O atom in PEO and the –OH group of PVA. Similar H-bonds form between the $–CONH_2$ group in PAM and the –COOH group in PAA. A complete description of all H-bonds that may form in these interfaces can be found in Fig. 1d. The initial structure of PEO was generated by the self-avoiding random walk approach with 60 repeat units per chain. Both LCO and SAM polymers were generated by our in-house code. Periodic boundary conditions were applied along all three directions. All material constituents including LCO, PEO and SAMs, were first fully equilibrated before being merged in VMD [43] to generate the LCO/PEO interface model. In each simulation system, the cross section is large enough to eliminate effects of the lateral size on interfacial thermal transport [18,44–46]. According to two previous studies on the graphene/PMMA interface and the α-Fe_2O_3 crystal, the lateral dimension of 35 Å is sufficient to yield converging thermal conductivity along the length direction which includes the contribution by all dominant phonon modes [44,46].

2.2. Molecular dynamics

MD simulation was performed using LAMMPS [47]. The LCO ionic crystal was modelled by Buckingham potential [48,49]. PEO and SAMs were described by the OPLSAA force field [50,51], which has been widely used to model polymers and their interfaces [52,53]. The non-bonded interaction between LCO and polymers was modelled by the universal force field (UFF) with potential parameters optimized to effectively characterize interfacial adhesion [54,55]. Initial molecular configurations were first minimized by conjugate gradient algorithm, and then equilibrated and annealed to eliminate residual stresses with a time step of 1 fs. During annealing, the system was heated up from

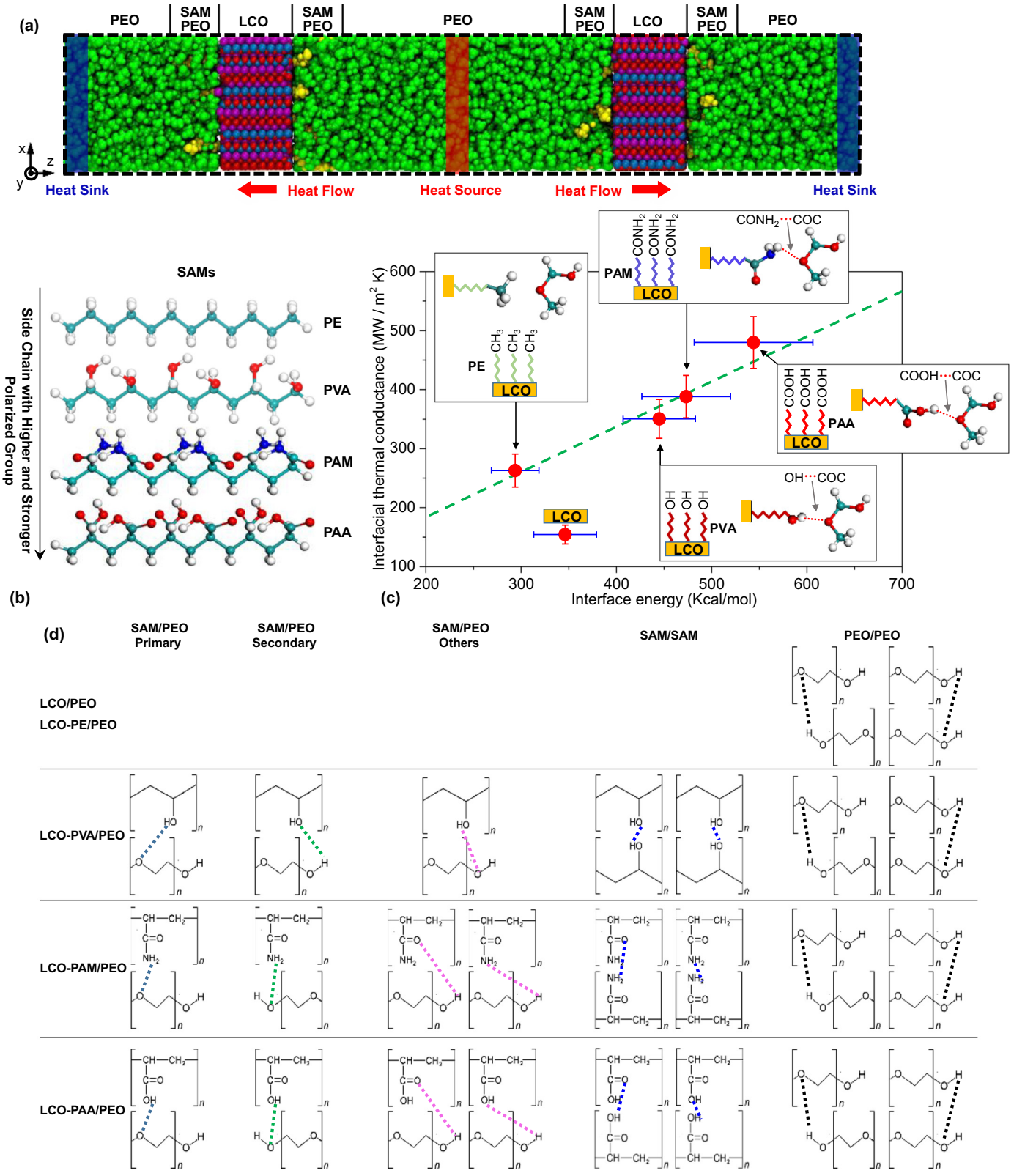

Fig. 1. (a) A full-atom model for calculating the interfacial thermal conductance between PEO and SAM-decorated LCO by using the reverse non-equilibrium molecular dynamics simulation. (b) Four polymers are considered as the decorative SAM: PE, PVA, PAM and PAA. (c) Interfacial thermal conductance and interfacial energy of adhesion across the pristine and four SAM-decorated LCO/PEO interfaces. Insets show schematics of the interfaces including the primary H-bond between PEO and the SAM. (d) A summary of all types of H-bonds (dashed lines) that may form in the materials systems under investigation. Rows show different materials systems including LCO/PEO, LCO-PE/PEO, LCO-PVA/PEO, LCO-PAM/PEO, and LCO-PAA/PEO. Columns show different groups of H-bonds in these systems including primary, secondary and other H-bonds between the SAM and PEO, H-bonds within the SAM, and H-bonds within PEO.

300 K to 500 K in 500 ps. The system was then relaxed at 500 K for 500 ps, cooled down to 300 K in 500 ps, and relaxed again at 300 K for 500 ps. The equilibrated structures were used in the subsequent simulation and analysis.

2.3. Interfacial thermal conductance

Interfacial thermal conductance was calculated based on the reverse non-equilibrium molecular dynamics (RNEMD) simulation. Using $G = J/\Delta T$, thermal conductance across the LCO/PEO interface can be calculated with the heat flux (J) and interfacial temperature drop (ΔT). The system setup can be found in Fig. 1a and Fig. S1a. The model was divided into 126 slabs along the direction of intended heat flow (i.e. the z-direction). The heat flow was generated by swapping the atomic kinematic energy of the coolest atoms in the "heat source" slab (red) and that of the hottest atoms in the "heat sink" slab (blue). Virtual elastic collision model was used to maintain momentum and energy conservation during velocity swapping. At steady state, the heat flux was calculated by $J = \Delta E/(2tA)$, where ΔE is the average energy exchange per swap, t is the time interval between swaps, A is the cross-sectional area, and the coefficient "2" accounts for the two symmetric conduction paths in the system. As shown in Fig. S1b, a temperature profile was obtained by evaluating the average temperature of all slabs. From the temperature profile, the temperature drop across the interface (ΔT) was evaluated. J together with ΔT gives G. In addition to giving G, the computational model also gives the thermal conductivity of PEO, which can be calculated by using $K = J/(\mathrm{d}T/\mathrm{d}z)$ where $\mathrm{d}T/\mathrm{d}z$ is the temperature gradient in PEO (found by the red lines in Fig. S1a). To verify the RNEMD calculation, G was also calculated by using non-equilibrium molecular dynamics (NEMD). The computational system for NEMD is shown in Fig. S1d. Temperature of the heat source was fixed at 320 K, while temperature of the heat sink was adjusted to make the interface temperature at approximately 300 K for all SAMs. Production runs of the RNEMD and NEMD simulation were 4 ns and 8 ns each with a time step of 1 fs.

2.4. Temperature field and atomic number density

NEMD was also employed to evaluate temperature and density distributions in the simulation box. For the calculation of temperature field, temperature of heat source and heat sink were fixed at 450 K and 250 K, respectively. Each model was first equally divided into 80 × 600 cells within the y-z plane. Atomic positions and velocities were collected during an interval of 4 ns after the steady state is reached. The temperature associated with all atoms inside a cell was averaged to find the cell temperature. The cell density was evaluated by counting all atoms in a cell. Cells not occupied by any atoms were given a temperature of zero.

2.5. Interfacial energy of adhesion

The interfacial energy of adhesion (W) was calculated to give its correlation with interfacial thermal conductance for different SAM-decorated interfaces. The calculation uses $W = (E_{LCO-SAM} + E_{PEO} - E_{all})/4$. Here, $E_{LCO-SAM}$ is the energy associated with the two SAM-decorated LCO blocks in the system as shown in Fig. 1a, E_{PEO} is the energy of the three PEO blocks, and E_{all} is the energy of the entire system. All of these energy terms were evaluated based on equilibrium MD simulation at 300 K with a time step of 0.5 fs, based on the full model (Fig. 1a) and partial models. The denominator of 4 accounts for the four interfaces included in the model.

2.6. Vibrational density of states (VDOS)

The VDOS analysis describes the atomic vibrational modes of materials, which can further be used to quantify the vibrational mismatch between two materials forming an interface. The VDOS was obtained by Fourier transform of the velocity autocorrelation function averaged over all atoms. It is defined as a function of frequency in the form of $\mathrm{VDOS}(f) = \int_0^{+\infty} e^{-i2\pi f\tau} C_v(\tau) d\tau$, where f is the frequency and τ is the autocorrelation time. $C_v(\tau)$ is the normalized velocity autocorrelation function defined by $C_v(\tau) = \frac{\langle \vec{v}(\tau)\cdot\vec{v}(0)\rangle}{\langle \vec{v}(0)\cdot\vec{v}(0)\rangle}$ where $\vec{v}(\tau)$ denotes the atomic velocity at the time of τ and $\langle\cdot\rangle$ represents an average over the entire system. To account for statistical randomness, the VDOS was evaluated by averaging twenty simulations that start from different initial velocities. Each simulation runs with a duration of 6.4 ns and a time step of 0.5 fs.

2.7. Cumulative correlation factor

To quantify the match or correlation between the vibrational modes of two materials forming an interface, a cumulative correlation factor (M) was defined as a function of the cutoff frequency, f_c. As an integration in the frequency domain from 0 to f_c, the cumulative correlation factor describes the vibrational match between two materials up to a specified cutoff frequency of f_c. The equation is $M(f_c) = \frac{\int_0^{f_c} \mathrm{VDOS_A}(f)\cdot\mathrm{VDOS_B}(f)df}{\int_0^{\infty}\mathrm{VDOS_A}(f)df\cdot\int_0^{\infty}\mathrm{VDOS_B}(f)df}$, where $\mathrm{VDOS_A}(f)$ and $\mathrm{VDOS_B}(f)$ are VDOS of the two materials, respectively. A lower M value indicates a lower match or a higher mismatch in the vibrational modes up to the frequency of f_c. When the cutoff frequency is greater or equal to the maximum frequency of all vibrational modes, the M factor is the same as the widely used correlation factor [56].

3. Results and discussion

3.1. Validation

The pristine LCO/PEO interface was simulated to validate MD calculations against experimental and computational results from literatures. First, the mass density of PEO was found to be about 1.18 g cm^{-3} at equilibrium, well within the range of 1.13–1.21 g cm^{-3} from the polymer database [57]. Secondly, the thermal conductivity of PEO was calculated to be 0.332 ± 0.015 W m^{-1} K^{-1}, which agrees well with the experimental results ranging from 0.20 to 0.37 W m^{-1} K^{-1} [58]. Thirdly, the thermal conductivity of LCO was calculated to be about 21.25 W m^{-1} K^{-1}, in good agreement with our previous EMD simulation results [59]. Lastly, thermal conductance across the pristine LCO/PEO interface calculated by the RNEMD method was found almost the same as that obtained by the NEMD method, with a minor difference of 8.45%.

3.2. H-bond dependent interfacial thermal conductance

Fig. 1c (vertical axis) plots the interfacial thermal conductance computed for various LCO/PEO interfaces, with error bars showing the standard deviation. Corresponding temperature profiles can be found in Fig. S2. The pristine LCO/PEO interface is shown to have an interfacial thermal conductance of 153.95 MW m^{-2} K^{-1}, lower than any SAM-functionalized interfaces. Among the four interfaces with SAMs, interfacial heat transfer is enhanced more by incorporating SAM molecules with stronger polarization. Ranking from the highest enhancement to the lowest is PAA, PAM, PVA and PE. Compared with the pristine interface, interfaces with these SAMs show interfacial thermal conductance enhanced by 211.69%, 151.99%, 127.36%, and 70.57%, respectively (i.e. from 153.95 MW m^{-2} K^{-1} to 479.84, 387.94, 350.02 and 262.59 MW m^{-2} K^{-1}). Note that the PE SAM does not form any H-bonds with PEO. The enhancement of 70.57% is solely due to the penetration of PE chains into the matrix, forming a thicker interface layer that bridges the distinct vibrational modes of LCO and PEO [34]. By comparison, the PAA, PAM and PVA SAMs all form hierarchical H-bond network at the interface as illustrated in Fig. 1a. Carried by SAMs that penetrate into the PEO, the massive number of H-bonds drastically

enhances the structural integrity of the interface, leading to enhanced thermal conductance.

3.3. Temperature field

The interfacial decoration with SAMs alleviates spatial discontinuities in the temperature field, thereby improving interfacial heat transfer. Fig. 2 plots the full temperature field computed for systems without and with different SAMs, where the same temperature difference is applied between the heat source and the heat sink. The pristine LCO/PEO system shows an obvious discontinuity (black ribbons in Fig. 2a) at the interface where no atoms exist due to the steric repulsion. By comparison, the discontinuity is partially removed in systems with SAMs. As shown in Fig. 2b–e, the black ribbons are relatively thinner and broken into pieces at the sites where SAMs exist. The partial removal of discontinuity implies that the incorporation of SAMs leads to new thermal transport pathways at the interface for more efficient heat transfer.

Moreover, SAMs also blend with PEO to form thick interfaces with high thermal conductivities. Fig. S3 shows line plots of the temperature profiles for systems under investigation. Overall, the pristine LCO/PEO interface shows a higher temperature drop than the other systems with SAMs, indicating inefficient interfacial heat transfer, echoing the results shown in Fig. 1c. More importantly, in Fig. S3, the SAM/PEO blending region is shown to have lower temperature gradients and therefore higher thermal conductivities than the region with PEO only. Despite the fact that PEO has similar thermal conductivities as the polymers used as SAMs in this study, two reasons make the blending region have higher thermal conductivities. On the one hand, H-bonds form between PEO and the SAMs including PVA, PAM and PAA. Similar to a previous study [60], H-bonds form thermal bridges between polymer chains and improve heat transfer in the polymer blends. On the other hand, the SAMs are relatively extended in the blending region. Studies have shown that extended polymer chains have drastically improved thermal conductivities along the chain direction than their amorphous counterparts [39,61]. As a result of both reasons combined, heat is conducted more efficiently in the blending region.

3.4. Stand-up chain morphology and atomic distribution

To verify that SAMs stand up in the blending zone, Fig. 3a–d plots the atomic number density distributions associated with LCO and the SAMs. One SAM chain is selected on each side of the LCO block. In contact with polymers, LCO shows slightly irregular density distribution at the left and right edges, mostly due to the surface energy. The functional SAMs including PE, PVA, PAM and PAA show stand-up configurations. The configuration is in part due to the steric repulsion between the SAM chains which forces the chains to be relatively straight. Moreover, H-bonds formed with the surrounding PEO further reinforce such configurations so that larger chain surfaces can be exposed to PEO for more H-bonds and lower system energy. The extended chain morphology of SAMs facilitates interfacial thermal conduction as it forces heat to be conducted along chain where thermal conduction is effective. Finally, the functional polymer chains show different widths due to their distinct side chains.

To further understand atomic distributions at the interface, Fig. 3e–h plots the atomic number density profiles of LCO, SAM and PEO for the four systems with SAMs, respectively. The irregular surface density distribution identified for LCO in Fig. 3a–d is shown more clearly here as two peaks near the interface. Due to the high stiffness of LCO, the peaks of LCO (blue lines) which are caused interfacial forces are shown to be very close for the four systems. By comparison, much more significant differences are found in the peaks of SAMs (green lines). PAA shows the highest peak density, followed by PAM, PVA, and PE. Within about 5 Å from the peak, the SAM density drops and reaches a plateau in all four systems. The difference in peak density of SAMs is in part due to the different average densities of these polymers with distinct side chains. It is also in part attributable to the different interactions between the SAMs and LCO. Finally, the different peaks in SAMs also disturb the distribution of PEO (red lines) in the SAM/PEO blending region, especially near LCO. Outside of the blending region, interfacial effects are minimal and the four systems show almost the same density for PEO.

3.5. Hierarchical hydrogen bonding network

As discussed above, the unique H-bond network enabled by SAMs partly removes discontinuity in the temperature field and straightens

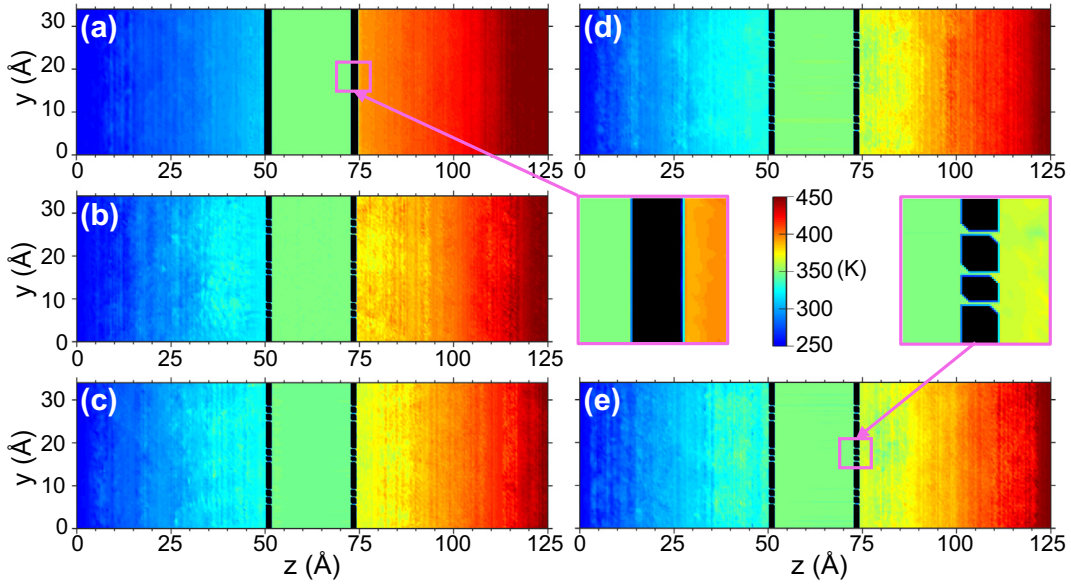

Fig. 2. Temperature contours of five simulation systems: (a) LCO/PEO, (b) LCO-PE/PEO, (c) LCO-PVA/PEO, (d) LCO-PAM/PEO and (e) LCO-PAA/PEO. The black belts are areas of effectively zero temperature as they are not occupied by atoms.

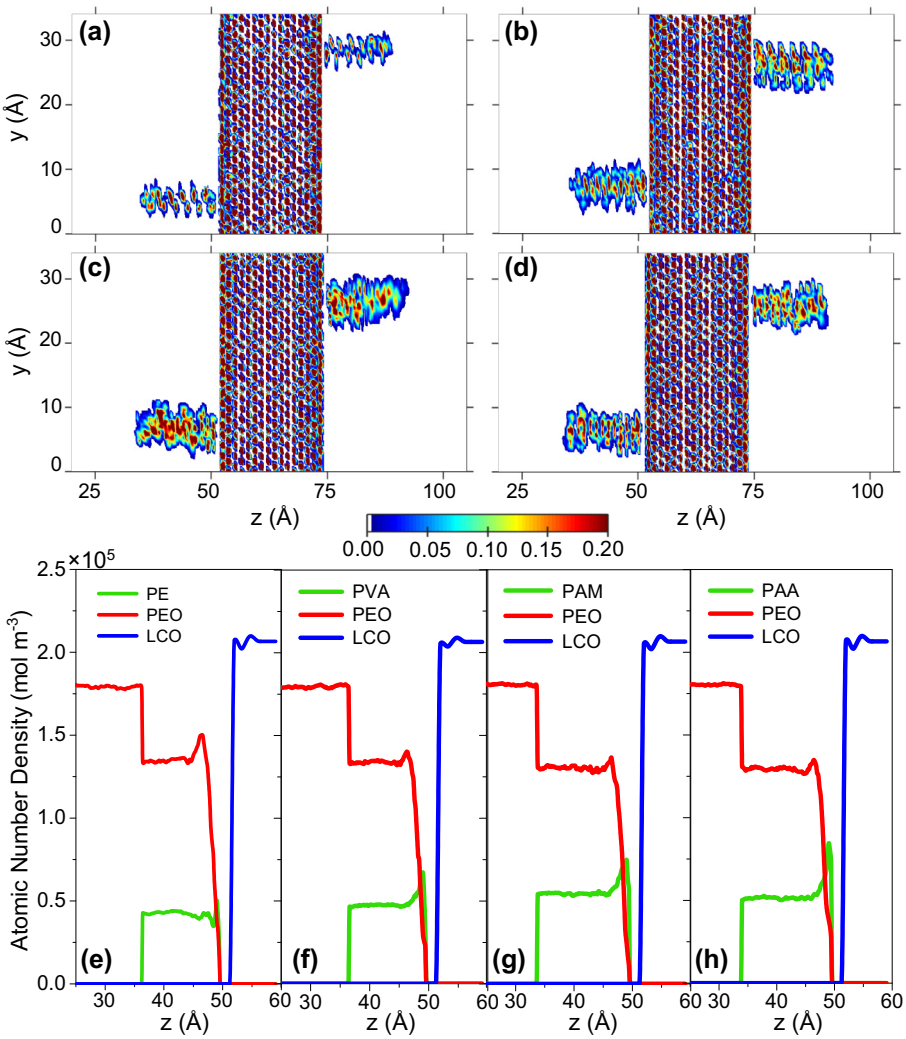

Fig. 3. Atomic number density distributions of LCO and SAMs for (a) LCO-PE/PEO, (b) LCO-PVA/PEO, (c) LCO-PAM/PEO and (d) LCO-PAA/PEO. One polymer chain is selected at each side of an interface as the representative. (e-h) Line plots of the atomic number density for the four systems.

functional polymer chains, both enhancing interfacial heat transfer. Despite sharing the same enhancement mechanism, the three SAM-functionalized interfaces with H-bonds show different levels of enhancement varying from 127.36% to 211.69% compared with the pristine LCO/PEO interface (Fig. 1c). Due to the crucial role of H-bonds, the different enhancement must be related with the H-bonds formed at the interface. To better understand H-bond formation, Fig. 4a–e plots the number of H-bonds versus time in all five systems at the steady state. A widely used geometric criterion is used to identify the H-bond. As shown in Fig. S4, a H-bond is established if: (1) the distance between the H-bond donor (D) and acceptor (A) is not longer than 3.0 Å; and (2) the angle between H-donor and H-acceptor is not larger than 20°. Note that neither the pristine LCO/PEO system nor the LCO-PE/PEO system gives zero H-bonds in the plot, because PEO chains by themselves can form H-bonds (Fig. 1d). Between the two systems, the pristine LCO/PEO has more H-bonds (8.45 ± 0.83 versus 6.30 ± 0.77) because more PEO is available in the system due to the lack of SAMs.

In the other three systems that have interfacial H-bonds (Fig. 4c–e), PAA gives the most H-bonds at the interface, followed by PAM and then PVA. The number of H-bonds formed within PEO is almost the same comparing the three systems. Note that all of these systems form multiple kinds of H-bonds. For example, the LCO-PAA/PEO system has -COOH···:O as the primary H-bond among the others including: (1) three other kinds formed between PAA and PEO, (2) two kinds formed within PAA, and (3) two kinds formed within PEO (see Fig. 1d for a complete list). The LCO-PAM/PEO system has –$CONH_2$···:O as the primary H-bond and seven others. The LCO-PVA/PEO interface has -OH···:O as the primary H-bond and six others. As shown in Fig. 4f, the primary H-bond accounts for about 80% of the total number of H-bonds formed at the interface.

To further illustrate how H-bonds form hierarchically in the extended chains of SAMs, Fig. 4g–i depicts H-bond distributions over 16,000 frames of MD simulation for each of the systems. With reference to Fig. 4f, four colors are used to show the primary (steel blue), secondary (green) and other (pink) H-bonds formed between SAM and PEO, and the H-bonds formed within SAM (royal blue), respectively. The H-bonds within PEO are not included as they do not participate in interfacial heat transfer directly. In all cases, H-bonds are well distributed along the SAM chains. The extended chain configuration allows larger exposure of SAM chains to PEO, leading to more H-bonds and making the SAM structure energetically more favorable. Between SAM and PEO, the primary H-bonds dominate with some secondary and other H-bonds scattered in between. In addition, H-bonds also form between neighboring SAM chains, although neighboring SAM chains have an average distance of 13.8 Å in the present setup. The unique H-bond structure displayed in these plots along with the steric repulsion makes the SAM chains highly extended.

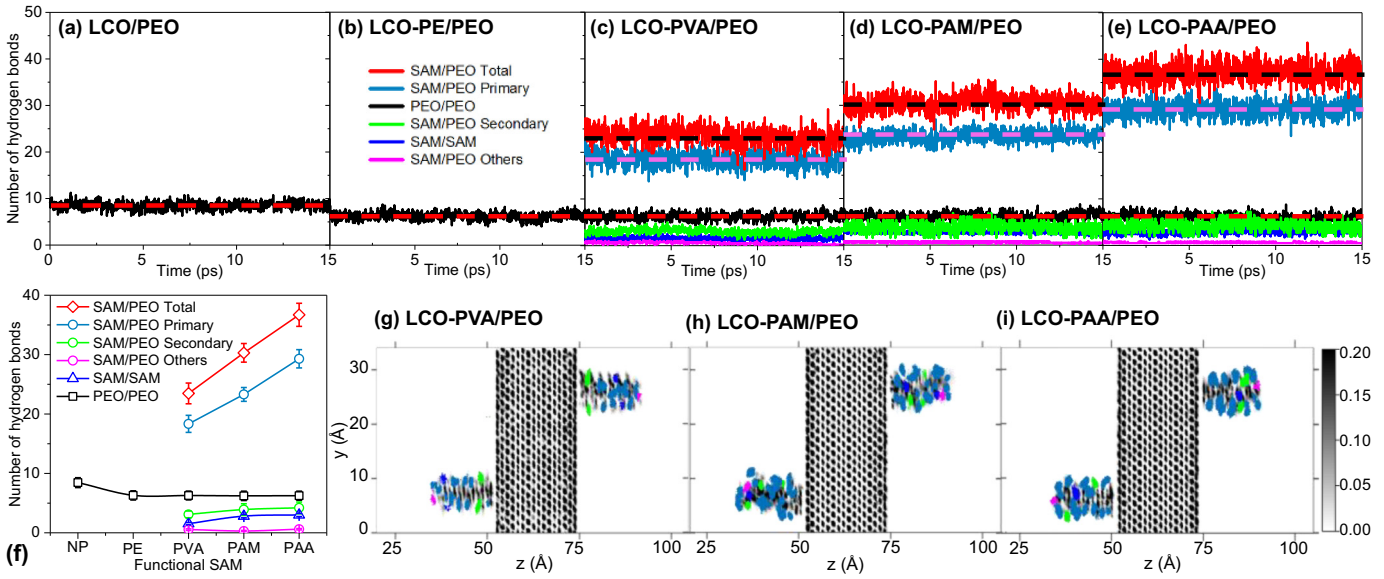

Fig. 4. Number of H-bonds versus time for (a) LCO/PEO, (b) LCO-PE/PEO, (c) LCO-PVA/PEO, (d) LCO-PAM/PEO and (e) LCO-PAA/PEO. H-bonds of different types are separately shown in the plots. Dashed lines indicate the averages. (f) Summary of the average number of H-bonds for the five systems. (g-i) Cloud maps of H-bond distributions. The grey cloud serves as the background showing the atomic distributions of LCO and SAMs. The colored clouds are H-bond distributions. Each dot in the cloud represents a H-bond forming in the position at a time instant. Colors match that used in (f): primary (steel blue), secondary (green) and other (pink) H-bonds between SAM and PEO; and H-bonds within or between SAM chains (blue). (For interpretation of the references to colour in this figure legend, the reader is referred to the web version of this article.)

3.6. Interfacial energy of adhesion

Previous studies in interfacial heat transfer have revealed a strong correlation between interfacial thermal conductance and interfacial energy of adhesion for a wide range of materials [15,62–64], with some exceptions [35]. To better understand the correlation for LCO/PEO interfaces, Fig. 1c plots the interfacial energy of adhesion in conjunction with the interfacial thermal conductance. The two quantities are found to be highly correlated for the four SAM-functionalized interfaces, showing an almost linear relationship (green dashed line in Fig. 1c). However, the pristine LCO/PEO interface is found to be an exception. Its adhesion energy is 17.89% higher than that of the PE-functionalized interface, while its interfacial thermal conductance is 41.37% lower. The result underlines the importance of structural similarity for the correlation rule to apply. Different from the interfaces with SAMs penetrating into the matrix, the pristine LCO/PEO interface features a bare flat interface leading to fundamentally different thermal transport mechanisms. The correlation rule breaks down as the thermal transport mechanism changes.

The H-bond plays a fundamental role in determining the interfacial energy of adhesion in the systems under investigation. Among the four interfaces with SAMs, the LCO-PE/PEO interface which has no H-bonds has the lowest energy of adhesion of 293.40 kcal/mol and the lowest interfacial thermal conductance of 262.59 MW m^{-2} K^{-1}. With hierarchical H-bonds, the LCO-PAA/PEO interface shows the highest energy of adhesion of 543.89 kcal/mol and the highest interfacial thermal conductance of 479.85 MW m^{-2} K^{-1}. From a chemistry point of view, the COOH···:O H-bond has a strength of 8.92 kcal/mol, followed by CONH···:O (7.40 kcal/mol) and OH···:O (5.0 kcal/mol). The higher bonding energy leads to a higher probability of forming a chemical bond. Hence, the LCO-PAA/PEO system, which has COOH···:O as the primary H-bond, shows the most H-bonds formed at the interface (Fig. 4). The larger number of H-bonds and the higher bonding strength per H-bond collectively cause the higher energy of adhesion at the PAA-decorated interface. The PAM and PVA-decorated interfaces have lower interfacial energy of adhesion and accordingly, lower interfacial thermal conductance.

3.7. Vibrational spectra coupling

SAM polymers enhance interfacial heat transfer as a vibrational mediator that modulate the vibrational coupling between LCO and PEO. According to the acoustic mismatch model and the diffusive mismatch model [46], interfacial thermal conductance is strongly correlated with the vibrational spectra coupling between two materials forming an interface [39,65]. The interfacial thermal conductance is usually higher when the two materials match more in their vibration modes [66]. Fig. 5a–e plots the VDOS of all components forming the five interfaces under investigation.

Without SAM decoration, the pristine LCO/PEO interface shows poor vibrational coupling as shown in Fig. 5f, which plots a LCO-PEO cumulative correlation factor. The poor coupling echoes the mismatch demonstrated in Fig. 5a, where PEO shows peaks around 37.45 THz and 90.67 THz while LCO shows peaks from 0 to 33 THz. By incorporating SAMs, vibrational match at the interface is drastically improved (Fig. 5b–e). For example, at the LCO-PAA/PEO interface (Fig. 5e), overlap of major peaks are identified at 41.36 and 90.97 THz. The improved vibrational match with SAMs is also evidenced in Fig. 5f, where SAM-decorated interfaces all show higher correlation than the pristine interface and the LCO-PAA/PEO interface with a strong H-bond network gives the highest interfacial correlation. Similar ranking are also found in the coupling between SAMs and PEO as plotted in Fig. 5g.

Interestingly, we note that even the same pair of materials, i.e. LCO and PEO, show different vibrational correlation factors in the presence of different SAMs (Fig. 5f). Vibrational energy transport is in essence wave transport underpinned by atomic vibrations. The process is highly sensitive to many factors. Materials composition is one of the most important factors, but structural and chemical environment is also critical. In this study, all systems under investigation have LCO and PEO in full or partial contact, where SAMs constitute the environment that influences materials behavior. With different SAMs, different types of H-bonds form in the systems and they influence wave transport and atomic vibrations. This is how the influence of SAMs on LCO/PEO correlation occurs.

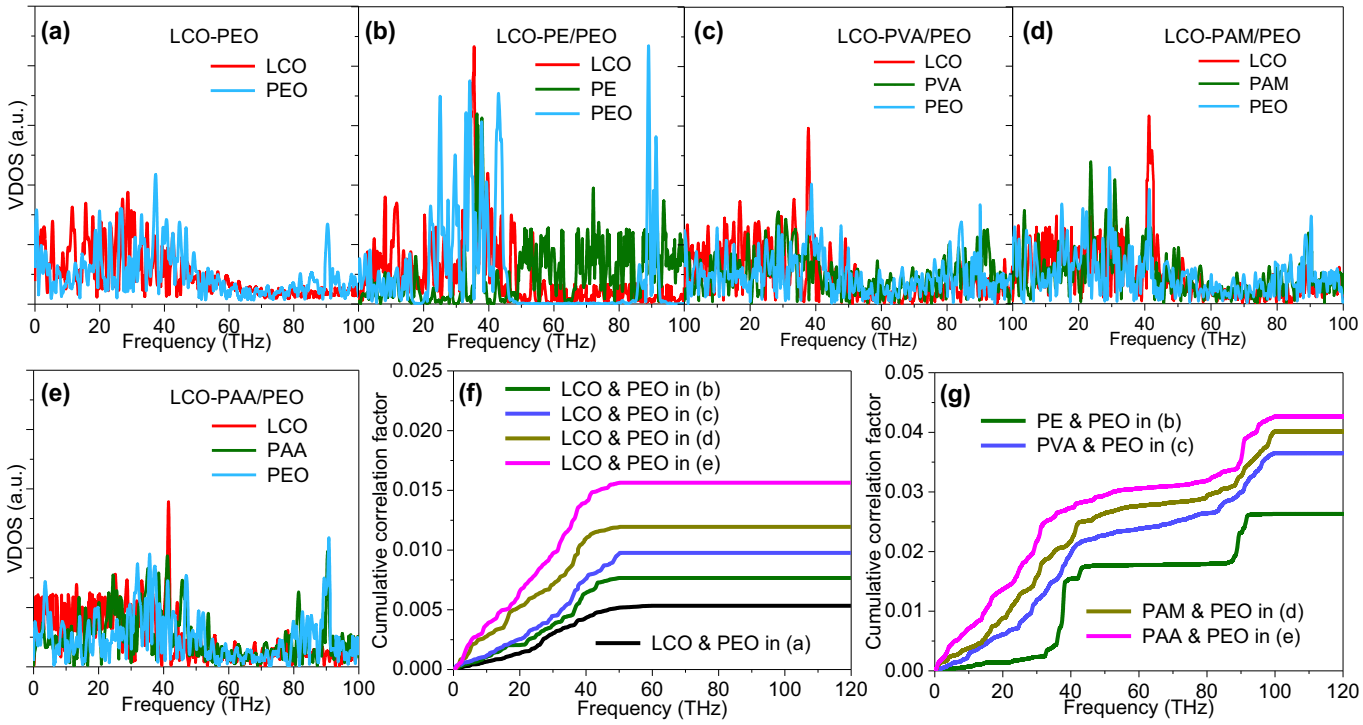

Fig. 5. Vibrational density of states (VDOS) of different components in (a) LCO/PEO, (b) LCO-PE/PEO, (c) LCO-PVA/PEO, (d) LCO-PAM/PEO and (e) LCO-PAA/PEO. (f) The cumulative correlation factor between LCO and PEO in the five systems. (g) The cumulative correlation factor between SAM and PEO in the four SAM-decorated systems.

4. Conclusions

Dictated by molecular design, the interface between LCO and PEO exhibits drastically different thermal conductance which has strong implications for heat removal and thermal management. H-bonded interfaces including LCO-PAA/PEO, LCO-PAM/PEO and LEO-PVA/PEO show enhancement of 211.69%, 151.99% and 127.36%, respectively, over the pristine interface. By comparison, LCO-PE/PEO which is a non-H-bonded interface enhances thermal conduction by 70.57% only. Apparently, the unique hierarchical H-bond network carried by SAMs is a primary contributor to the significantly enhanced interfacial thermal conduction. The contribution strongly depends on the type, location and density of H-bonds. As revealed in the plot of H-bond clouds, multiple types of H-bonds coexist in each of the systems under investigation. The primary H-bond, which usually accounts for about 80% of all H-bonds at the interface, largely determines the interfacial energy of adhesion and interfacial thermal conductance. For example, the LCO-PAA/PEO interface which features a strong primary H-bond, -COOH···:O, has the interfacial thermal conductance 211.69% and the interfacial energy 57.24% more than the pristine interface. The two physical quantities show a linear relationship for the four SAM-decorated interfaces, while the pristine interface which has fundamentally different thermal transport mechanisms disobeys the rule. All SAM-decorated interfaces are shown to have: (1) alleviated discontinuities in the temperature field, (2) stand-up configurations with extended chains, and (3) enhanced coupling of vibrational modes. They synergistically improve interfacial thermal transport, in which H-bonds play a positive role. The H-bond-governed interfacial thermal transport has been previously shown to depend on the density of SAMs [34,60], and is envisioned to be influenced by the length of SAMs as well which will be a topic of future investigation. The results are expected to improve fundamental understanding and applications of H-bonded interface engineering for improved thermal management of multi-material systems including the lithium-ion batteries.

Declaration of Competing Interest

The authors declare no competing financial interest.

Acknowledgement

This work is financially supported by CAREER Award No. CBET-1751610 from the National Science Foundation, United States. The authors would like to thank Dr. Zheyong Fan of Aalto University for fruitful discussion. This research made use of the resources of the High Performance Computing Center at Idaho National Laboratory, United States, which is supported by the Office of Nuclear Energy of the U.S. Department of Energy and the Nuclear Science User Facilities under Contract No. DE-AC07-05ID14517.

Appendix A. Supplementary data

Representative RNEMD and NEMD simulation systems and associated temperature profiles (Fig. S1); Temperature profiles for five LCO/PEO systems calculated with RNEMD (Fig. S2) and NEMD (Fig. S3); Criteria for identifying hydrogen bonds (Fig. S4). Supplementary data to this article can be found online at https://doi.org/10.1016/j.matdes.2020.108927.

References

[1] J.B. Bates, N.J. Dudney, B. Neudecker, A. Ueda, C.D. Evans, Thin-film lithium and lithium-ion batteries, Solid State Ionics 135 (1) (2000) 33–45.
[2] H. Wang, X. Cao, W. Liu, X. Sun, Research Progress of the solid state Lithium-sulfur batteries, Front. Energy Res. 7 (112) (2019).
[3] Z. Qiu, Y. Zhang, S. Xia, P. Dong, Research Progress on Interface properties of inorganic solid state lithium ion batteries, Acta Chimica Sinica -Chinese Edition 73 (2015) 992–1001.
[4] J.-Y. Liang, X.-X. Zeng, X.-D. Zhang, P.-F. Wang, J.-Y. Ma, Y.-X. Yin, X.-W. Wu, Y.-G. Guo, L.-J. Wan, Mitigating interfacial potential drop of cathode–solid electrolyte

via ionic conductor layer to enhance interface dynamics for solid batteries, J. Am. Chem. Soc. 140 (22) (2018) 6767–6770.
[5] T. Inoue, K. Mukai, Are all-solid-state Lithium-ion batteries really safe?–verification by differential scanning calorimetry with an all-inclusive microcell, ACS Appl. Mater. Interfaces 9 (2) (2017) 1507–1515.
[6] B. Li, M.H. Parekh, R.A. Adams, T.E. Adams, C.T. Love, V.G. Pol, V. Tomar, Lithium-ion battery thermal safety by early internal detection, prediction and prevention, Sci. Rep. 9 (1) (2019), 13255. .
[7] T.M. Bandhauer, S. Garimella, T.F. Fuller, A critical review of thermal issues in lithium-ion batteries, J. Electrochem. Soc. 158 (3) (2011) R1–R25.
[8] H. Chung, B. Kang, Mechanical and thermal failure induced by contact between a Li1.5Al0.5Ge1.5(PO4)3 solid electrolyte and Li metal in an all solid-state Li cell, Chem. Mater. 29 (20) (2017) 8611–8619.
[9] J.B. Goodenough, K.-S. Park, The Li-ion rechargeable battery: a perspective, J. Am. Chem. Soc. 135 (4) (2013) 1167–1176.
[10] P.J. O'Brien, S. Shenogin, J. Liu, P.K. Chow, D. Laurencin, P.H. Mutin, M. Yamaguchi, P. Keblinski, G. Ramanath, Bonding-induced thermal conductance enhancement at inorganic heterointerfaces using nanomolecular monolayers, Nat. Mater. 12 (2012) 118.
[11] S. Kaur, N. Raravikar, B.A. Helms, R. Prasher, D.F. Ogletree, Enhanced thermal transport at covalently functionalized carbon nanotube array interfaces, Nat. Commun. 5 (2014) 3082.
[12] J.P. Reifenberg, K. Chang, M.A. Panzer, S. Kim, J.A. Rowlette, M. Asheghi, H.P. Wong, K.E. Goodson, Thermal boundary resistance measurements for phase-change memory devices, IEEE Electron Device Lett. 31 (1) (2010) 56–58.
[13] V. Vishwakarma, C. Waghela, Z. Wei, R. Prasher, S.C. Nagpure, J. Li, F. Liu, C. Daniel, A. Jain, Heat transfer enhancement in a lithium-ion cell through improved material-level thermal transport, J. Power Sources 300 (2015) 123–131.
[14] T. Liu, S.-Y. Yue, S. Ratnasingham, T. Degousée, P. Varsini, J. Briscoe, M.A. McLachlan, M. Hu, O. Fenwick, Unusual thermal boundary resistance in halide Perovskites: a way to tune ultralow thermal conductivity for thermoelectrics, ACS Appl. Mater. Interfaces 11 (50) (2019) 47507–47515.
[15] K. Zheng, F. Sun, X. Tian, J. Zhu, Y. Ma, D. Tang, F. Wang, Tuning the interfacial thermal conductance between polystyrene and sapphire by controlling the interfacial adhesion, ACS Appl. Mater. Interfaces 7 (42) (2015) 23644–23649.
[16] H. Xu, X. Zhang, G. Hu, L. Weng, L. Liu, High thermal conductivity EP adhesive based on the GO/EP interface optimized by TDI, Polym. Adv. Technol. 31 (6) (2020) 1356–1364.
[17] M. Hu, P. Keblinski, P.K. Schelling, Kapitza conductance of silicon–amorphous polyethylene interfaces by molecular dynamics simulations, Phys. Rev. B 79 (10) (2009), 104305. .
[18] M. Shen, W.J. Evans, D. Cahill, P. Keblinski, Bonding and pressure-tunable interfacial thermal conductance, Phys. Rev. B 84 (19) (2011), 195432. .
[19] Y. Zhang, H. Han, N. Wang, P. Zhang, Y. Fu, M. Murugesan, M. Edwards, K. Jeppson, S. Volz, J. Liu, Improved heat spreading performance of functionalized graphene in microelectronic device application, Adv. Funct. Mater. 25 (28) (2015) 4430–4435.
[20] M.D. Losego, M.E. Grady, N.R. Sottos, D.G. Cahill, P.V. Braun, Effects of chemical bonding on heat transport across interfaces, Nat. Mater. 11 (2012) 502.
[21] S. Majumdar, J.A. Sierra-Suarez, S.N. Schiffres, W.-L. Ong, C.F. Higgs, A.J.H. McGaughey, J.A. Malen, Vibrational mismatch of metal leads controls thermal conductance of self-assembled monolayer junctions, Nano Lett. 15 (5) (2015) 2985–2991.
[22] M. Hu, J.V. Goicochea, B. Michel, D. Poulikakos, Water Nanoconfinement induced thermal enhancement at hydrophilic quartz interfaces, Nano Lett. 10 (1) (2010) 279–285.
[23] M. Wang, N. Hu, L. Zhou, C. Yan, Enhanced interfacial thermal transport across graphene–polymer interfaces by grafting polymer chains, Carbon 85 (2015) 414–421.
[24] Y. Wang, H.F. Zhan, Y. Xiang, C. Yang, C.M. Wang, Y.Y. Zhang, Effect of covalent functionalization on thermal transport across graphene–polymer interfaces, J. Phys. Chem. C 119 (22) (2015) 12731–12738.
[25] J. Mosnáček, A. Popelka, J. Osicka, J. Filip, M. Ilcikova, J. Kollar, A.B. Yousaf, T. Bertok, J. Tkac, P. Kasak, Modulation of wettability, gradient and adhesion on self-assembled monolayer by counterion exchange and pH, J. Colloid Interface Sci. 512 (2018) 511–521.
[26] R. Schoeppner, C. Ferguson, L. Pethö, C. Guerra-Nuñez, A.A. Taylor, M. Polyakov, B. Putz, J.-M. Breguet, I. Utke, J. Michler, Interfacial adhesion of alumina thin films over the full compositional range of ternary fcc alloy films: a combinatorial nanoindentation study, Mater. Des. 193 (2020), 108802. .
[27] K. Chu, X.-h. Wang, Y.-b. Li, D.-j. Huang, Z.-r. Geng, X.-l. Zhao, H. Liu, H. Zhang, Thermal properties of graphene/metal composites with aligned graphene, Mater. Des. 140 (2018) 85–94.
[28] X. Qiu, V. Ivasyshyn, L. Qiu, M. Enache, J. Dong, S. Rousseva, G. Portale, M. Stöhr, J.C. Hummelen, R.C. Chiechi, Thiol-free self-assembled oligoethylene glycols enable robust air-stable molecular electronics, Nat. Mater. 19 (3) (2020) 330–337.
[29] T. Minamiki, Y. Ichikawa, R. Kurita, Systematic investigation of molecular recognition ability in FET-based chemical sensors functionalized with a mixed self-assembled monolayer system, ACS Appl. Mater. Interfaces 12 (13) (2020) 15903–15910.
[30] W.-C. Lan, T.-S. Huang, Y.-C. Cho, Y.-T. Huang, C. Walinski, P.-C. Chiang, M. Ruslin, F.-T. Pai, C.-C. Huang, M.-S. Huang, The potential of a nanostructured titanium oxide layer with self-assembled monolayers for biomedical applications: surface properties and biomechanical behaviors, Appl. Sci. 10 (2020) 590.
[31] M. Gärtner, Understanding the properties of tailor-made self-assembled monolayers with embedded dipole moments for Interface engineering, J. Phys. Chem. 122 (50) (2018) 28757–28774 (2018 v.122 no.50).
[32] M. Singh, N. Kaur, E. Comini, The role of self-assembled monolayers in electronic devices, J. Mater. Chem. C 8 (12) (2020) 3938–3955.
[33] X. Wang, X. Liu, H. Yuan, H. Liu, C. Liu, T. Li, C. Yan, X. Yan, C. Shen, Z. Guo, Non-covalently functionalized graphene strengthened poly(vinyl alcohol), Mater. Des. 139 (2018) 372–379.
[34] L. Zhang, L. Liu, Polymeric self-assembled monolayers anomalously improve thermal transport across graphene/polymer interfaces, ACS Appl. Mater. Interfaces 9 (34) (2017) 28949–28958.
[35] T. Zhang, A.R. Gans-Forrest, E. Lee, X. Zhang, C. Qu, Y. Pang, F. Sun, T. Luo, Role of hydrogen bonds in thermal transport across hard/soft material interfaces, ACS Appl. Mater. Interfaces 8 (48) (2016) 33326–33334.
[36] L. Zhang, M. Ruesch, X. Zhang, Z. Bai, L. Liu, Tuning thermal conductivity of crystalline polymer nanofibers by interchain hydrogen bonding, RSC Adv. 5 (107) (2015) 87981–87986.
[37] L. Zhang, Z. Bai, H. Ban, L. Liu, Effects of the amino acid sequence on thermal conduction through β-sheet crystals of natural silk protein, Phys. Chem. Chem. Phys. 17 (43) (2015) 29007–29013.
[38] L. Zhang, T. Chen, H. Ban, L. Liu, Hydrogen bonding-assisted thermal conduction in β-sheet crystals of spider silk protein, Nanoscale 6 (14) (2014) 7786–7791.
[39] Y. Xu, X. Wang, J. Zhou, B. Song, Z. Jiang, E.M.Y. Lee, S. Huberman, K.K. Gleason, G. Chen, Molecular engineered conjugated polymer with high thermal conductivity, Sci. Adv. 4 (3) (2018) eaar3031.
[40] X. Wei, T. Zhang, T. Luo, Thermal energy transport across hard–soft interfaces, ACS Energy Lett. 2 (10) (2017) 2283–2292.
[41] J.-C. Lai, L. Li, D.-P. Wang, M.-H. Zhang, S.-R. Mo, X. Wang, K.-Y. Zeng, C.-H. Li, Q. Jiang, X.-Z. You, J.-L. Zuo, A rigid and healable polymer cross-linked by weak but abundant Zn(II)-carboxylate interactions, Nat. Commun. 9 (1) (2018) 2725.
[42] K. Mizushima, P.C. Jones, P.J. Wiseman, J.B. Goodenough, LixCoO2 (0<x⩽1): a new cathode material for batteries of high energy density, Solid State Ionics 3–4 (1981) 171–174.
[43] W. Humphrey, A. Dalke, K. Schulten, VMD: Visual molecular dynamics, J. Mol. Graph. 14 (1) (1996) 33–38.
[44] H. Kim, A.A. Abdala, C.W. Macosko, Graphene/polymer Nanocomposites, Macromolecules 43 (16) (2010) 6515–6530.
[45] S. Majumdar, J.A. Malen, A.J.H. McGaughey, Cooperative molecular behavior enhances the thermal conductance of binary self-assembled monolayer junctions, Nano Lett. 17 (1) (2017) 220–227.
[46] J. Severin, P. Jund, Thermal conductivity calculation in anisotropic crystals by molecular dynamics: application to α—Fe2O3, J. Chem. Phys. 146 (5) (2017), 054505. .
[47] S. Plimpton, Fast parallel algorithms for short-range molecular dynamics, J. Comput. Phys. 117 (1) (1995) 1–19.
[48] F.X. Hart, J.B. Bates, Lattice model calculation of the strain energy density and other properties of crystalline LiCoO2, J. Appl. Phys. 83 (12) (1998) 7560–7566.
[49] G.V. Lewis, C.R.A. Catlow, Potential models for ionic oxides, J. Phys. C Solid State Phys. 18 (6) (1985) 1149–1161.
[50] W.L. Jorgensen, D.S. Maxwell, J. Tirado-Rives, Development and testing of the OPLS all-atom force field on conformational energetics and properties of organic liquids, J. Am. Chem. Soc. 118 (45) (1996) 11225–11236.
[51] M.L.P. Price, D. Ostrovsky, W.L. Jorgensen, Gas-phase and liquid-state properties of esters, nitriles, and nitro compounds with the OPLS-AA force field, J. Comput. Chem. 22 (13) (2001) 1340–1352.
[52] R. Godawat, S.N. Jamadagni, S. Garde, Characterizing hydrophobicity of interfaces by using cavity formation, solute binding, and water correlations, Proc. Natl. Acad. Sci. 106 (36) (2009), 15119. .
[53] S. Kuang, J.D. Gezelter, Simulating interfacial thermal conductance at metal-solvent interfaces: the role of chemical capping agents, J. Phys. Chem. C 115 (45) (2011) 22475–22483.
[54] F. Sun, T. Zhang, M.M. Jobbins, Z. Guo, X. Zhang, Z. Zheng, D. Tang, S. Ptasinska, T. Luo, Molecular bridge enables anomalous enhancement in thermal transport across hard-soft material interfaces, Adv. Mater. 26 (35) (2014) 6093–6099.
[55] A.K. Rappe, C.J. Casewit, K.S. Colwell, W.A. Goddard, W.M. Skiff, UFF, a full periodic table force field for molecular mechanics and molecular dynamics simulations, J. Am. Chem. Soc. 114 (25) (1992) 10024–10035.
[56] B. Li, J. Lan, L. Wang, Interface thermal resistance between dissimilar anharmonic lattices, Phys. Rev. Lett. 95 (10) (2005), 104302. .
[57] J.E. Mark, Physical Properties of Polymer Handbook, 2007.
[58] C. Lu, S.W. Chiang, H. Du, J. Li, L. Gan, X. Zhang, X. Chu, Y. Yao, B. Li, F. Kang, Thermal conductivity of electrospinning chain-aligned polyethylene oxide (PEO), Polymer 115 (2017) 52–59.
[59] J. He, L. Zhang, L. Liu, Thermal transport in monocrystalline and polycrystalline lithium cobalt oxide, Phys. Chem. Chem. Phys. 21 (23) (2019) 12192–12200.
[60] L. Zhang, L. Liu, Hierarchically hydrogen-bonded graphene/polymer interfaces with drastically enhanced interfacial thermal conductance, Nanoscale 11 (8) (2019) 3656–3664.
[61] Y. Xu, D. Kraemer, B. Song, Z. Jiang, J. Zhou, J. Loomis, J. Wang, M. Li, H. Ghasemi, X. Huang, X. Li, G. Chen, Nanostructured polymer films with metal-like thermal conductivity, Nat. Commun. 10 (1) (2019) 1771.
[62] T. Luo, J.R. Lloyd, Enhancement of thermal energy transport across graphene/graphite and polymer interfaces: a molecular dynamics study, Adv. Funct. Mater. 22 (12) (2012) 2495–2502.

[63] N. Shenogina, R. Godawat, P. Keblinski, S. Garde, How wetting and adhesion affect thermal conductance of a range of hydrophobic to hydrophilic aqueous interfaces, Phys. Rev. Lett. 102 (15) (2009), 156101. .

[64] L. Zhang, Z. Bai, L. Liu, Exceptional thermal conductance across hydrogen-bonded graphene/polymer interfaces, Adv. Mater. Interfaces 3 (13) (2016) 1600211.

[65] X. Liu, J. Gao, G. Zhang, Y.-W. Zhang, Design of phosphorene/graphene heterojunctions for high and tunable interfacial thermal conductance, Nanoscale 10 (42) (2018) 19854–19862.

[66] D.G. Cahill, P.V. Braun, G. Chen, D.R. Clarke, S. Fan, K.E. Goodson, P. Keblinski, W.P. King, G.D. Mahan, A. Majumdar, H.J. Maris, S.R. Phillpot, E. Pop, L. Shi, Nanoscale thermal transport. II. 2003–2012, Appl. Phys. Rev. 1 (1) (2014), 011305. .